Additive Manufacturing 36 (2020) 101548

Contents lists available at ScienceDirect

Additive Manufacturing

journal homepage: www.elsevier.com/locate/addma

The deformation and elastic anisotropy of a new gyroid-based honeycomb made by laser sintering

I. Maskery*, I.A. Ashcroft

Centre for Additive Manufacturing, University of Nottingham, Nottingham NG8 1BB, UK

ARTICLE INFO

Keywords:
Gyroid
Lattice
Honeycomb
Powder bed fusion
Anisotropy

ABSTRACT

The stiffness, anisotropy and structural deformation of three gyroid-based lattices was investigated, with particular focus on a newly proposed honeycomb gyroid. This honeycomb is based on a modified triply periodic minimal surface (TPMS) equation with reduced periodicity. Using the numerical homogenisation method, the anisotropy of the gyroid lattice types was found to differ greatly, as was the dependence of this anisotropy on the volume fraction. From compression testing of laser sintered polyamide PA2200 specimens, the honeycomb gyroid was found to possess extremely high anisotropy, with $E^*_{\max}/E^*_{\min}$, the ratio of the highest to the lowest direction-dependent modulus, ~ 250 at low volume fraction. The stiffness and anisotropy of the honeycomb gyroid are compared to equivalent results from the square honeycomb, the closest analogue in the set of conventional honeycomb types. The honeycomb gyroid lattice exhibited novel deformation and post-yield stiffening under in-plane loading; it underwent reorientation into a second, stiffer geometry following plastic bending and contact of its cell walls. The unique deformation behaviour and extremely high anisotropy of the honeycomb gyroid provide strong motivation for further investigations into this new family of reduced periodicity TPMS-based honeycombs.

1. Introduction

Lattice structure performance has become an important element of design for additive manufacturing (DfAM). This is because AM lattices are an example of cellular structures, a class of materials known to possess high specific mechanical properties [1,2]. Other motivating factors for the study of AM lattices include their application in impact protection [3,4], thermal management [5,6], tissue engineering [7–10] and vibration control [11–15].

There are several aspects of AM lattice performance which are under-investigated, but could lead to new DfAM approaches as well as useful new forms of structural response. One overlooked aspect of lattice performance is mechanical anisotropy, which has been observed in materials made using a range of AM processes [16–19], and is often associated with the layer-by-layer fabrication process and part orientation during fabrication [20–24]. For DfAM, a more important contribution to the mechanical anisotropy of a lattice is the intrinsic anisotropy of the constituent cells. Xu et al. [25] examined a range of lattice types of varying complexity, providing clear evidence that their stiffness is generally direction-dependent, and that this anisotropy can be controlled through manipulation of the lattice geometry. Dong et al. [26] demonstrated lattice anisotropy control through the selection of cell type and volume fraction, before presenting a method to compensate for the intrinsic anisotropy of lattice cells using multiple materials. More recently, Cutolo et al. [27] found that the mechanical properties and failure modes of the triply periodic minimal surface (TPMS) diamond lattice were significantly affected by the loading direction with respect to the lattice orientation.

Tancogne-Dejean and Mohr [28] found that the body-centred cubic (BCC) lattice exhibited $E^*_{\max}/E^*_{\min}$ (the ratio of the highest to the lowest direction-dependent modulus) of close to 20 at low volume fraction. Lu et al. [29] and Soyarslan et al. [30] independently used the numerical homogenisation method to examine the anisotropy of several TPMS scaffolds, which they expressed through the Zener ratio. Soyarslan et al. [30] found this to reach up to approximately 4.5 for the I-WP lattice type at a volume fraction of 0.15. Such findings highlight the importance of lattice anisotropy for DfAM. Lattice stiffness has so far been prescribed principally through the choice of volume fraction. Establishing lattice anisotropy as a major consideration in DfAM opens the possibility of maximising a latticed component's stiffness through cellular orientation, without increasing its mass.

Another aspect of AM lattice design which has received little attention is the prospect of structures with novel deformation and stiffening mechanisms. Lattice structures with graded strut or wall

---

* Corresponding author.
E-mail address: ian.maskery@nottingham.ac.uk (I. Maskery).

https://doi.org/10.1016/j.addma.2020.101548
Received 7 April 2020; Received in revised form 22 July 2020; Accepted 12 August 2020
Available online 21 August 2020
2214-8604/

thickness have been shown to exhibit sequential layer collapse under compressive loads, giving rise to characteristic staircase features in their stress-strain curves [31–34]. There is also some evidence that lattice grading can be used to avoid low-strain failure modes such as diagonal shear [33,32] and enhance the absorption of deformation energy compared to non-graded structures [31,32,35,36], though the extent of these effects seems highly dependent on the lattice cell type.

It is with the aim of uncovering new forms of mechanical response in AM lattices, and incorporating these into useful design methods, that this investigation of lattice stiffness, anisotropy and deformation is presented. Three lattice types, all based on the gyroid TPMS, were investigated. Two of these, the network and matrix gyroid, have been examined previously by Maskery et al. [37,38], while the third, the honeycomb gyroid, is believed to be a new and valuable contribution to the field, as it possesses very high mechanical anisotropy and displays a structural reconfiguration and post-yield stiffening unlike the 3D periodic lattices generally considered for AM applications. The deformation behaviour of this new gyroid-based honeycomb is also significantly different from that of the AM hexagonal honeycomb examined by Weidmann et al. [39], who provided a comprehensive assessment of that structure's manufacturability by metal laser powder bed fusion, as well as in-plane stiffness determined by beam-theory, finite element modeling and experiment.

The specimens in this study were manufactured by the laser sintering (LS) process from the polymer PA2200, also known as nylon 12. The post-yield behaviour of the honeycomb gyroid lattice was examined in particular detail, this being important for the design of efficient impact-absorbing structures such as armour panels.

Our methodology concerning lattice design, numerical analysis and mechanical testing is presented in Section 2. Our results are presented in Section 3. Discussion and conclusions are found in Sections 4 and 5, respectively.

2. Methodology

This section details the methods used to design the gyroid-based lattice structures based on their surface equations, estimate their direction-dependent elastic moduli, and investigate their deformation under compressive loading.

First, some elementary nomenclature regarding lattice design and performance are introduced. The volume fraction (or relative density) of a lattice structure is given by

$$\rho^* = \frac{\rho_{\mathrm{latt}}}{\rho_{\mathrm{sol}}}, \tag{1}$$

where ρ_{latt} and ρ_{sol} are the densities of the lattice structure and the constituent materials, respectively. ρ^* takes values from 0 to 1, where 1 represents a fully solid structure. Similarly, the relative elastic modulus of a lattice structure is expressed as

$$E^* = \frac{E_{\mathrm{latt}}}{E_{\mathrm{sol}}}, \tag{2}$$

where E_{latt} and E_{sol} are the elastic moduli of the lattice structure and the constituent material, respectively. In general, E^* is related to ρ^* through the Gibson–Ashby relationship [1]:

$$E^* = C_1 \rho^{*n}. \tag{3}$$

The prefactor C_1 was given by Gibson, Ashby et al. as a range of values from 0.1 to 4.0, while $n \approx 2$ when deformation occurs by bending of the cellular struts or walls [1,2]. Our previous work [37] and that of others [40,41] has indicated that n may be closer to unity when the lattice deformation is stretching- rather than bending-dominated.

2.1. Gyroid lattice structure design

Network and matrix gyroid lattice structures were generated using approximations of their TPMS functions. These comprise the leading term of a trigonometric Fourier series, as described by Gandy et al. [42]. A shorthand notation for sine and cosine functions is defined, such that

$$S_i = \sin\left(2\pi n_i \frac{i}{L_i}\right) \tag{4}$$

and

$$C_i = \cos\left(2\pi n_i \frac{i}{L_i}\right), \tag{5}$$

where $i = x$, y, z, and L_i and n_i are the dimensions of the lattice and numbers of cell repetitions in each direction, respectively. Gyroid lattice structures were then determined by finding the $U = 0$ isosurface of [42]

$$U_{\mathrm{gyr}} = (S_x C_y + S_y C_z + S_z C_x)^n - t^n, \tag{6}$$

where t is an arbitrary parameter used to control the volume fraction of the resulting structure.

The exponent n in Eq. (6) can take the value of 1, designating the network structure, or 2, the matrix. The network structure contains two continuous regions of space separated by the $U = 0$ surface, one of which is designated ‘solid’ and one ‘void’ for the purpose of AM lattice structure design. The matrix structure contains three separate regions; two of equal size and equivalent geometry divided by a third in the form of a continuous wall. This separating wall is treated as the solid region. Matrix lattices have also been referred to as ‘shell’-type, ‘sheet’-type and ‘shellular’ lattices in the literature [43–48].

A new surface equation based on Eq. (6) but lacking the terms which are periodic in z may be introduced:

$$U_{\mathrm{hon}} = (S_x C_y + S_y + C_x)^2 - t^2. \tag{7}$$

Eq. (7) separates space into one continuous wall-like region and an array of non-connected regions, the number of which is determined by the lattice periodicities in x and y. Designating the continuous region to be solid and the non-connected regions to be void results in a honeycomb which, like most repeating lattices considered for AM, has tailorable unit cell dimensions and volume fraction. Therefore, the TPMS equations which have received a great deal of attention recently for AM lattice design, can, with simple modification, be used to create a new family of surface-based honeycombs.

Correlations between the t parameters of Eqs. (6) and (7) and ρ^* for the network, matrix and honeycomb gyroid lattices are presented in Fig. 1, while Fig. 2 illustrates their form. Henceforth, the lattice structure arising from Eq. (7) is referred to as the honeycomb gyroid.

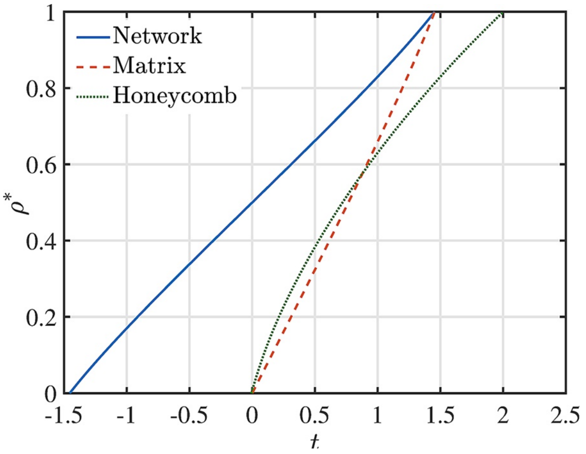

Fig. 1. Relationships between the t parameter of Eqs. (6) and (7) and ρ^* for network, matrix and honeycomb gyroid lattices.

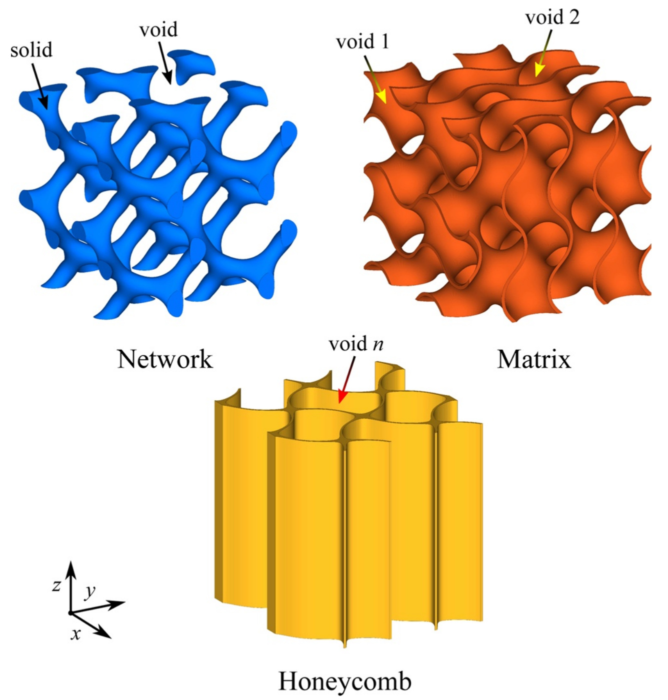

Fig. 2. Unit cell geometries based on the gyroid surface. For the network and matrix lattices, the illustrations show 2 × 2 ×2 configurations of unit cells, while the honeycomb has 2 × 2 cells.

2.2. Homogenisation and elastic anisotropy

To estimate the stiffness anisotropy of each gyroid-based lattice, the 3D finite element (FE) homogenisation approach of Dong et al. [26] was used. This computes the homogenised stiffness matrix, C^H, for a given lattice unit cell, and is similar to the homogenisation solution for 2D periodic structures proposed by Andreassen and Andreassen [49].

Dong et al. provided a MATLAB code for their homogenisation method called `homo3D`, which takes as inputs the first and second Lamé parameters of the lattice constitutive material, and a representation of the lattice unit cell as a voxel model. In this work, voxel models of network, matrix and honeycomb gyroid unit cells were obtained from the relevant $U = 0$ isosurfaces (Eqs. (6) and (7)), in the same way as was shown previously by Maskery et al. [37]. The `homo3D` code was previously used by Nguyen et al. [50] to obtain effective material properties for AM lattice structures, and was found to be accurate in predicting the elastic load-deflection response of a 3-point bend experiment.

The first and second Lamé parameters are given by

$$\lambda = \frac{\nu E}{(1+\nu)(1-2\nu)} \tag{8}$$

and

$$\mu = \frac{E}{2(1+\nu)}, \tag{9}$$

respectively, where E is the elastic modulus of the lattice constitutive material, and ν its Poisson's ratio. For comparison with compressive testing of AM fabricated lattice specimens, these material properties were defined to be those of LS PA2200. For the Poisson's ratio the value of 0.3 [51] was taken, while for the elastic modulus the value of 1.695 GPa was used, which is an average of PA220 tensile and compressive moduli from solid specimens made using the same LS machine and powder feedstock as used here [37]. This combination of E and ν was previously used in FE lattice models and was found to predict the stiffness of LS specimens reasonably well, with the difference in numerical and experimental results being attributed to the tension-compression modulus anisotropy of LS PA2200 and the effect of surface roughness [37]. Based on these material properties, the first and second Lamé parameters are 0.978 GPa and 0.652 GPa, respectively.

Once C^H was obtained from the `homo3D` code, its inverse provided the homogenised compliance matrix S^H. The elastic moduli of the lattice structure along the [100], [010] and [001] directions are found from:

$$E_{[100]} = \frac{1}{S_{11}^H}, \tag{10a}$$

$$E_{[010]} = \frac{1}{S_{22}^H}, \tag{10b}$$

$$E_{[001]} = \frac{1}{S_{33}^H}, \tag{10c}$$

while the moduli along other relevant high symmetry directions are found from [52]:

$$\frac{1}{E_{[110]}} = S_{11}^H - \frac{1}{2}\left[(S_{11}^H - S_{12}^H) - \frac{1}{2}S_{44}^H\right], \tag{11a}$$

$$\frac{1}{E_{[111]}} = S_{11}^H - \frac{2}{3}\left[(S_{11}^H - S_{12}^H) - \frac{1}{2}S_{44}^H\right]. \tag{11b}$$

([001], [110], etc. are standard notation for directions in cubic crystal systems. [100], [010] and [001] are analogous to the x, y and z directions, respectively, while [110] refers to the ‘edge’ direction halfway between x and y, and [111] is a ‘corner’ direction inclined by 35.3° toward z from [110]. The reader is directed to Maskery et al. [53], in particular figure 8 of that work, for further information on how these directions relate to cubic lattice structures.)

The Zener ratio, α_r, may also be determined from C^H. This quantifies the degree of elastic anisotropy in a structure or material, and is defined as [54]

$$\alpha_r = \frac{2C_{44}^H}{C_{11}^H - C_{22}^H}, \tag{12}$$

where C_{44}^H is the resistance to shear across the (100) plane in an arbitrary direction, and $(C_{11}^H - C_{22}^H)/2$ is the resistance to shear across the (110) plane along the $[1\bar{1}0]$ direction. A perfectly isotropic material or structure will have $\alpha_r = 1$, with larger deviations from unity representing more elastic anisotropy.

Like other FE methods, the `homo3D` numerical homogenisation method is sensitive to the discretisation of the input voxel model [26]. It was found that, for each of the examined lattice types at a volume fraction of 0.2, $E_{[001]}$ was well converged when the unit cell voxel model was discretised with a mesh of around 50 elements along each axis. This is in good agreement with Dong et al.'s conclusion on the same topic [26]. To ensure accuracy, the anisotropy results presented in this paper were obtained from models discretised with 70 elements along each axis. For unit cells of volume fraction 0.1, this corresponds to around 35,000 elements, while for unit cells of volume fraction 0.4, this corresponds to around 140,000 elements.

Lattice anisotropy may be effectively conveyed with a 3D modulus surface. Representative surfaces for the network, matrix and honeycomb gyroid lattices are shown in Fig. 3. Visual inspection reveals the matrix gyroid lattice to be the most isotropic, as reflected in the near-sphericity of its modulus surface. The honeycomb gyroid is the most anisotropic, possessing extremely high modulus along the z direction (generally called *out-of-plane*) compared to the xy-plane (*in-plane*). This is quantified more thoroughly in Section 3.3.

2.3. Fabrication and testing

Gyroid lattice specimens measuring 50 mm × 50 mm × 50 mm were fabricated using an EOS P100 laser sintering machine, with

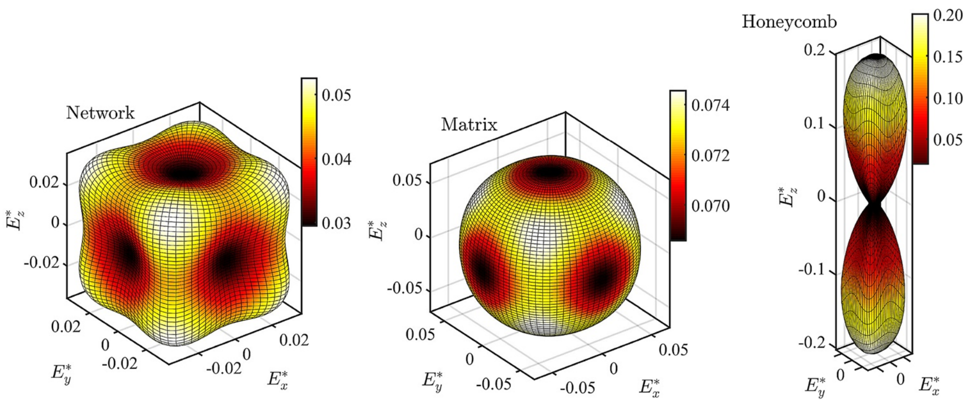

Fig. 3. Homogenised relative elastic moduli, E^*, for the network (left), matrix (centre) and honeycomb (right) gyroid lattice of volume fraction 0.2.

Table 1
LS parameters used in the production of lattice structures for mechanical testing.

LS parameter	
Laser power	21 W
Laser scan speed	2500 mm/s
Laser hatch spacing	250 µm
Powder bed temperature	173 °C
Powder deposition thickness	100 µm

processing parameters given in Table 1. The specimens were made from polyamide PA2200. Solid specimens manufactured alongside the lattices were used to determine the density of the LS PA2200 material. Comparison of specimen masses and volumes yielded a density of 960 kg/m^3, which agrees well with the material provider's specifications [55] and indicates minimal residual porosity. Network and matrix gyroid lattices comprised 5 × 5 × 5 unit cells, while honeycomb gyroid lattices had 5 × 5 unit cells. After manufacture the specimens were weighed, yielding an average volume fraction of 0.162 ± 0.003. This is slightly larger than the target volume fraction of 0.15, and is most likely a consequence of partially-sintered powder adhered to the internal lattice surfaces. The impact of this additional powder on the mechanical properties of the fabricated lattice structures is expected to be minimal.

Network and matrix gyroid specimens are shown in Fig. 4(a), while honeycomb gyroid specimens are shown in Fig. 4(b). To investigate stiffness anisotropy in the honeycomb gyroid lattice and to examine the compressive failure modes of this new lattice type, honeycomb lattices were manufactured in two orientations; they were made with their cellular [001] and [100] directions, respectively, aligned with the LS build direction. Thus, any stiffness anisotropy between these directions will be attributable solely to the intrinsic anisotropy of the honeycomb, not the anisotropy resulting from layer-by-layer LS fabrication. Network and matrix gyroid lattices were made with their [111] cellular directions aligned vertically, as these orientations were predicted by the homogenisation method (and shown in Fig. 3) to provide the highest stiffness for these structures.

To obtain stress–strain curves and investigate their failure modes, the fabricated gyroid lattice specimens were subject to compressive mechanical testing. This utilised an Instron 5966 universal testing machine equipped with a 50 kN load cell. The deformation rate was 0.25 mm/s, and a video camera was used to record the lattice deformation during the tests.

2.4. Finite element analysis

Finite element (FE) analysis was used to investigate cellular deformation in the honeycomb gyroid lattice under loading along the [100] direction. This lattice was modelled with a ten-node tetrahedral FE mesh (C3D10 elements) with general contact enabled, and the results were obtained using the Abaqus/Standard 2018 solver (Dassault Systemes – Vélizy-Villacoublay, France). The elements were assigned an elastic-plastic material model, with the yield strain and hardening determined by our previously reported experimental data for LS PA2200 [37], and a Poisson's ratio of 0.3 [51].

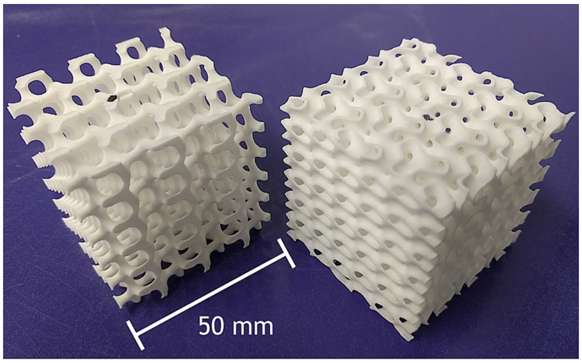

(a) Network (left) and matrix (right) gyroid lattice structures with their [111] cellular directions aligned vertically.

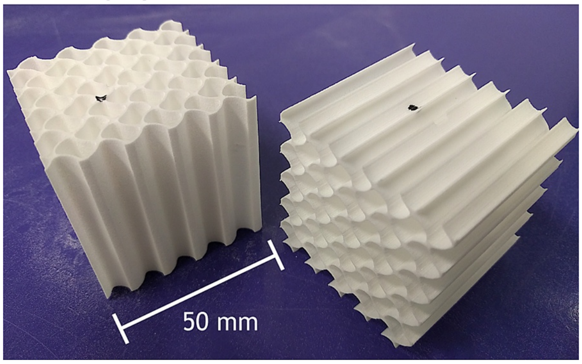

Fig. 4. Lattice specimens fabricated by laser sintering. Black marks on the specimens indicate the upward facing surfaces during fabrication.

The honeycomb lattice FE model had a 4 × 4 arrangement of cells and dimensions of 5 mm × 40 mm × 40 mm. Owing to the 2D, rather than 3D, periodicity of the honeycomb lattice, a lower thickness was specified in the x direction. This allowed for a finer FE mesh than would be practicable modelling a larger, cubic structure, whilst providing an accurate depiction of the deformation in the yz-plane. The total number of elements in the model was around 1.4 million. Displacement loads were applied uniformly to all nodes at the top surface of the FE model, while the *ZSYMM* boundary condition (translation in the xy-plane only and rotation around z only) was applied at the bottom surface.

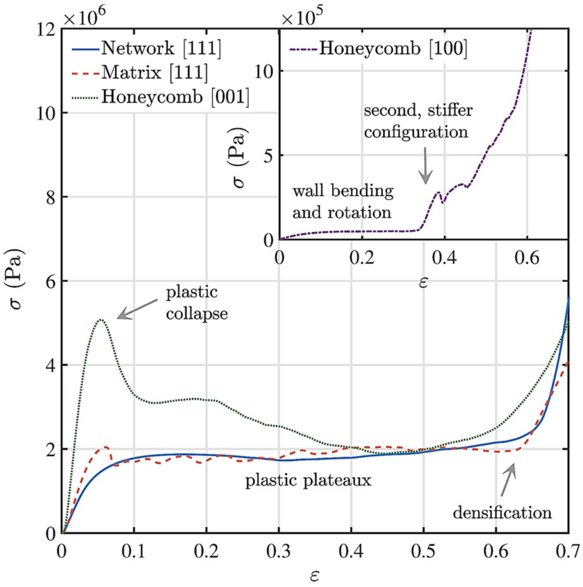

Fig. 5. Stress–strain curves of network, matrix and honeycomb gyroid lattices with volume fraction 0.15.

3. Results

3.1. Lattice deformation under compression

Stress–strain curves corresponding to fabricated network, matrix and honeycomb gyroid lattices with volume fraction 0.15 are shown in Fig. 5.

The network and matrix gyroid lattices exhibited the fairly typical stress-strain curves of cellular structures composed of elastic–plastic material; they showed an initial elastic response (from which $E_{\text{latt.}}$ is determined) followed by long plastic plateaux and eventual densification, where the lattice struts or walls are forced into direct contact. The deformation of the honeycomb gyroid lattice under [001] loading was similar, but is marked by a significant reduction in strength following the onset of plastic collapse at $\varepsilon \approx 0.05$, and a further strength reduction at $\varepsilon \approx 0.2$. Plastic collapse, likely following localised buckling of the honeycomb cell walls, was evident in the deformation video frames for this structure at $\varepsilon = 0.075$, as shown in Fig. 6.

The honeycomb lattice under [100] loading initially showed the typical stress-strain response of the other structures, but underwent significant stiffening at $\varepsilon \approx 0.35$, as shown in Fig. 5 (inset). This stiffening continued under further deformation, until the densification mechanism dominated at high strain. An explanation for this stress-strain response is seen in the video frames of Fig. 7. Following initial elasticity, deformation occurred through the gradual rotation and plastic bending of the curved honeycomb walls in the yz-plane. By $\varepsilon = 0.3$, this bending and rotation almost reached its limit, with the cell walls bent by almost 90° at their mid-points. Between $\varepsilon = 0.3$ and $\varepsilon = 0.4$ the bent cell walls came into contact with those of neighbouring cells. This restricted further deformation in the yz-plane by the cell wall bending and rotation mechanism.

This cell rotation and wall-contact stiffening mechanism is supported by FE analysis; von Mises stress distributions in the honeycomb lattice under increasing compressive strain are shown in Fig. 8. Between $\varepsilon = 0.1$ and $\varepsilon = 0.3$ the honeycomb gyroid cell walls underwent plastic bending (the plastic yield strength of the constituent material is approximately 30 MPa). By $\varepsilon = 0.4$ many of the cell walls came into contact with those of their neighbours. By $\varepsilon = 0.5$ this was true of most of the cell walls, and the stress distributed through the thicker lattice 'nodes', the regions at which the cell walls meet, was much greater than at lower strain, though still below the plastic yield strength. Based on this result, and the video deformation shown above, it is believed the rapid stiffening shown in Fig. 5 (inset) is consistent with the reorientation of the honeycomb gyroid lattice into a second configuration between $\varepsilon = 0.3$ and $\varepsilon = 0.4$, and the transition from bending- to stretching-dominated deformation.

3.2. Honeycomb gyroid stiffness

Wang and McDowell summarised analytic relationships for the in-plane relative moduli of a several conventional honeycomb structures at low density, including those based on repeating square, triangular and hexagonal cells [56]. Of most relevance to this work are Wang and McDowell's results for the square cell. They gave [56]

$$E^*_{\text{dia}} = \frac{1}{4}\rho^{*3}, \tag{13}$$

for in-plane diagonal loading, while loading along the x or y directions resulted in

$$E^*_x = E^*_y = \frac{1}{2}\rho^*. \tag{14}$$

These scaling relationships are relevant here because the connectivity of the square cell is the same as that of the honeycomb gyroid lattice; i.e., four walls connecting perpendicularly at each lattice node. The similarity in their form is illustrated in Fig. 9(a) (for convenience, the square cell is shown rotated by 45 degrees compared to the conventional orientation). The square cell density-modulus relationships of (13) and (14) are shown in Fig. 9(b), in which direct comparison can be made with the equivalent relationships for the gyroid honeycomb determined from numerical homogenisation.

The honeycomb gyroid results shown in Fig. 9(b) were obtained with fitting functions of the form $E^* = C_1\rho^{*n} + E^*_0$, the Gibson-Ashby scaling relationship for cellular structures with an additional term to account for systematic uncertainties in the determination of E^* by the numerical homogenisation method. Directional Young's moduli $E^*_{[100]}$ and $E^*_{[110]}$ were extracted from the homogenised compliance matrices for honeycomb gyroid cells with $\rho^* = 0.1 - 0.4$, using Eqs. (10a) and (11a). The resulting parameters for these density-modulus relationships are given in Table 2. From these parameters it can be deduced that; (i) the in-plane stiffness of the honeycomb gyroid has a greater dependence on the volume fraction than even the square honeycomb loaded in the diagonal direction (i.e., the ρ^* exponents are greater than 3), and

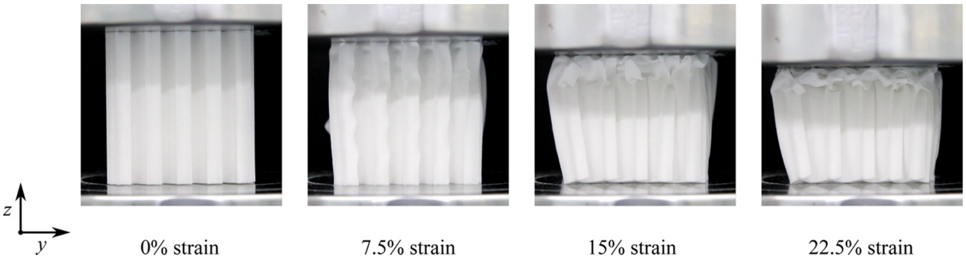

Fig. 6. Deformation of the honeycomb gyroid lattice under [001] compressive loading.

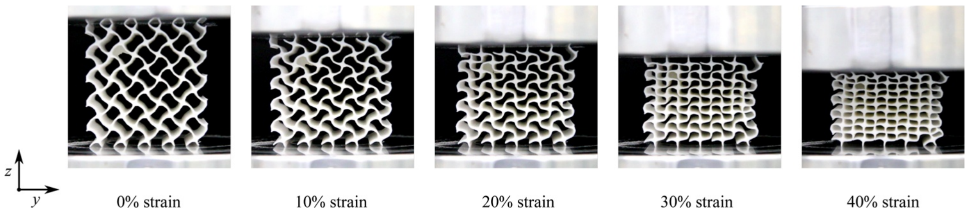

Fig. 7. Deformation of the honeycomb gyroid lattice under [100] compressive loading.

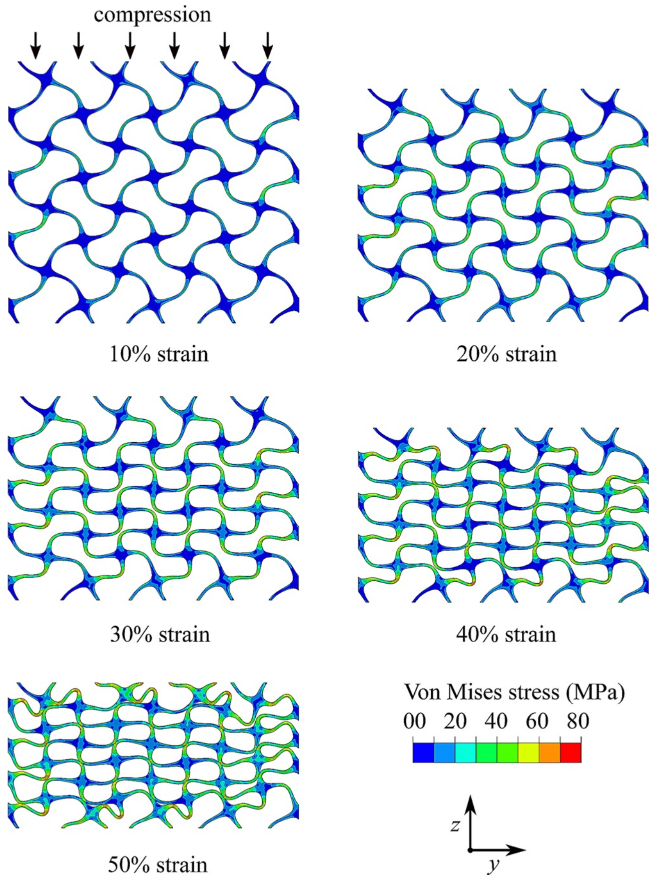

Fig. 8. Deformation (and von Mises stresses) of the honeycomb gyroid lattice under [100] compressive loading according to FE analysis.

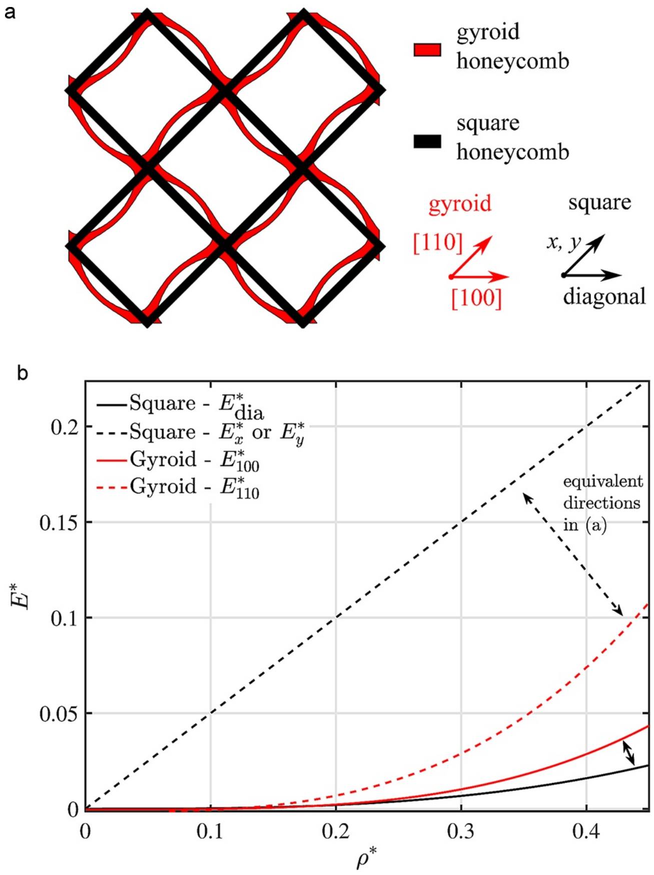

Fig. 9. The gyroid and square honeycombs compared; (a) their geometries, and (b) their in-plane density-modulus scaling relationships.

(ii) the in-plane stiffness of the honeycomb gyroid is less anisotropic than that of the square honeycomb. The issue of anisotropy is explored further in the following section. Also in Table 2 are the $E^*_{[001]}$ fitting results for the honeycomb gyroid from numerical homogenisation. These show a linear relationship with volume fraction, which is the typical out-of-plane behaviour shared by other honeycombs [1]. E^*_0 in all cases was found to be ∼0, indicating that systematic uncertainties were negligible.

3.3. Gyroid lattice anisotropy

The relative elastic moduli of the examined lattice structures are given in Table 3. Based on compression testing, the honeycomb lattice loaded in the [001] direction was the stiffest of the examined structures, having a modulus around three times greater than the matrix gyroid lattice loaded in its stiffest direction. In contrast, the relative elastic modulus of the honeycomb lattice in the [100] direction was extremely small, giving $E^*_{\mathrm{max}}/E^*_{\mathrm{min}} = 250 \pm 10$. This measure of anisotropy was previously used by Tancogne-Dejean and Mohr [28], who found $E^*_{\mathrm{max}}/E^*_{\mathrm{min}} = 18.2$ for the BCC lattice structure at a volume fraction of 0.1.

Table 2
Gibson–Ashby model parameters for the honeycomb gyroid along different loading directions. The model function is $E^* = C_1\rho^{*n} + E^*_0$.

Direction	C_1	n	$E^*_0 \times 10^{-3}$
[100]	0.73 ± 0.08	3.5 ± 0.1	−0.3 ± 0.3
[110]	1.4 ± 0.3	3.2 ± 0.3	−2 ± 2
[001]	1	1	0

Table 3
Relative elastic moduli of lattice structures at a volume fraction of 0.15, as determined by compression of fabricated specimens.

	$E^* \times 10^{-3}$
Network [111]	22.9 ± 0.1
Matrix [111]	33.3 ± 0.5
Honeycomb [001]	98 ± 5
Honeycomb [100]	0.389 ± 0.009

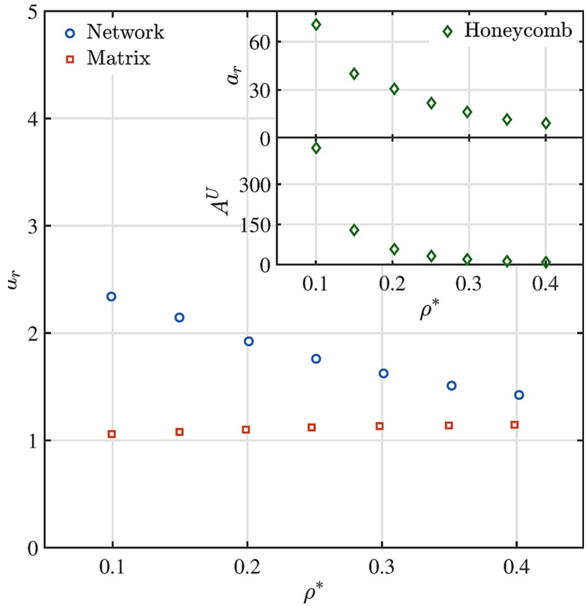

Fig. 10. Anisotropy of the three examined gyroid lattice types.

Zener ratios, α_r, for the network, matrix and honeycomb lattices determined using the numerical homogenisation method are shown in Fig. 10. For the matrix gyroid, α_r took values close to unity, and increased slightly to 1.1, over the range $\rho = 0.1–0.4$, in agreement with the previous result of Chen et al. [52]. α_r for the network gyroid decreased from 2.3 at $\rho^* = 0.1$ to 1.4 at $\rho^* = 0.4$, which closely agrees with the result of Lu et al. [29].

The honeycomb gyroid lattice had $\alpha_r = 71$ at $\rho^* = 0.1$, which decreased rapidly to $\alpha_r = 9.3$ at $\rho^* = 0.4$. Volume fraction therefore provides a sensitive control parameter for mechanical anisotropy in this new honeycomb structure. The function $\alpha_r = B\rho^{*c}$, with $B = 3.25$ and $c = -1.34$ provided a good description of α_r for the honeycomb gyroid over $\rho^* = 0.1–0.4$. However, it should be noted that the honeycomb gyroid does not possess the cubic spatial symmetry for which the Zener ratio was originally introduced. For this reason, the universal anisotropy index, A^U, was also calculated for the honeycomb gyroid. This measure of anisotropy was developed by Ranganathan and Ostoja-Starzewski [57] as a generalistion of the Zener ratio to quantify crystal elastic anisotropy. A^U for the honeycomb gyroid, presented in the inset to Fig. 10, also exhibits a decreasing trend with volume fraction, with the dependence described by $A^U = D\rho^{*f}$, with $D = 0.49$ and $f = -2.95$. These relationships for $\alpha_r(\rho^*)$ and $A^U(\rho^*)$ can henceforth be used to specify a volume fraction to provide a required level of anisotropy from the honeycomb gyroid; though evidently they must be elucidated if they are to be used at higher volume fractions.

With respect to in-plane anisotropy, Gibson and Ashby [1] usefully compared the elastic modulus of several common honeycomb types; the square, the triangle and the hexagon. This is illustrated in the polar plot of Fig. 11(a), which shows the directional relative moduli for square, triangular and hexagonal honeycombs with $t/l = 0.2$, with t and l being the thickness and length of the honeycomb walls, respectively. The volume fraction of the square honeycomb is given by $\rho^* = 2t/l$, meaning that this takes the value 0.4 in Fig. 11(a). For comparison, equivalent results are presented in Fig. 11(b) for the honeycomb gyroid with volume fractions from 0.15 to 0.4. The in-plane modulus of the honeycomb gyroid is evidently more isotropic than that of the square honeycomb, and far less isotropic than those of the triangular and hexagonal honeycombs.

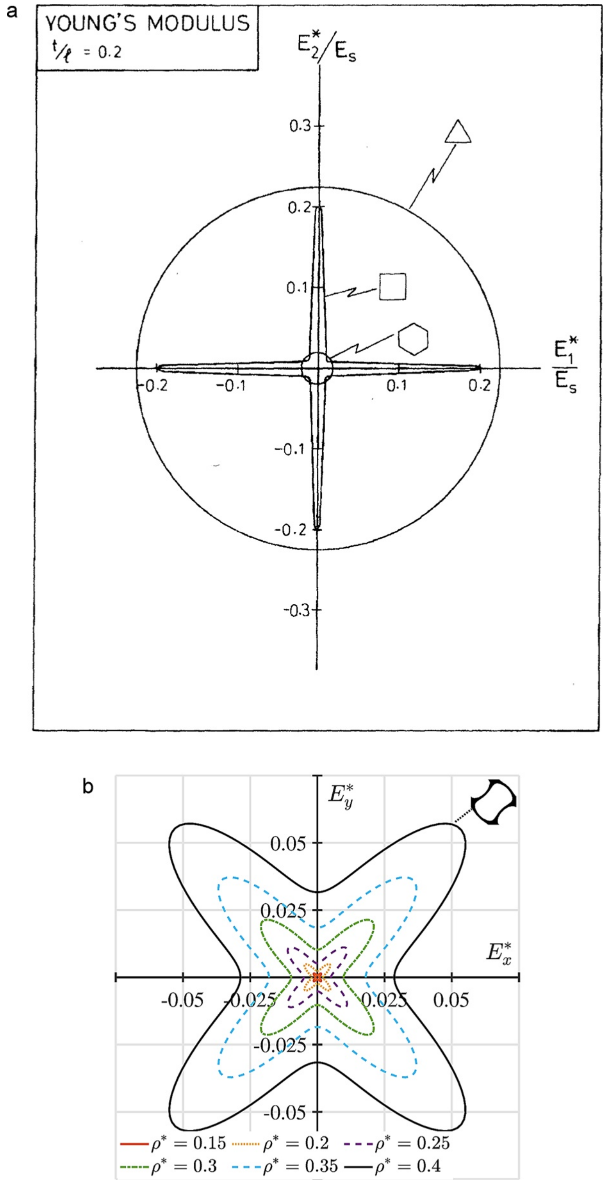

Fig. 11. Comparison of in-plane modulus for common honeycomb types; square, triangle and hexagon (a), with the honeycomb gyroid (b). Results for the honeycomb gyroid were obtained by numerical homogenisation.

3.4. Hybrid honeycomb lattice structures

The results in Section 3.1 show that the newly proposed honeycomb gyroid lattice, unlike the more commonly studied triply periodic network and matrix gyroid lattices, possesses very high mechanical anisotropy as well as unique structural reconfiguration and post-yield stiffening under in-plane loading. This is extremely attractive for impact protection panels or armour, in which post-yield stiffening leads to greater energy absorption and can help prevent the penetration of an impactor. Hybrid AM lattices featuring stiff and more compliant regions may provide a means to design such energy-absorbing structures. For this reason, two hybrid lattice structures based on the honeycomb gyroid were designed, fabricated and subject to the same compressive testing as the other lattice types examined above. The hybrid structures featured either two or three regions in which the orientation of the honeycomb was varied. In the two-layer hybrid, the orientation of the honeycomb was [100] in the bottom half of the structure and [001] in the top half. In the three-layer hybrid, the orientation was [100] in the top and bottom thirds, and [001] in the middle third. The hybrid

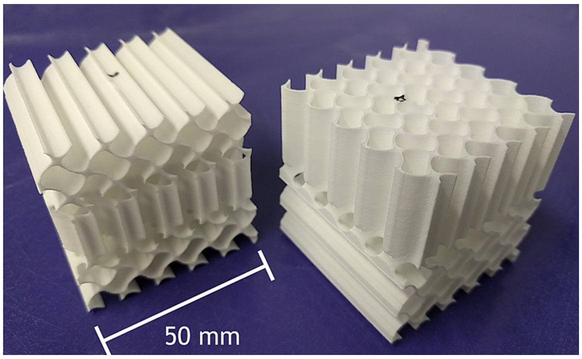

Fig. 12. Three-layer (left) and two-layer (right) hybrid honeycomb gyroid lattices. Black marks on the specimens indicate the upward facing surfaces during fabrication.

structures are shown in Fig. 12.

The three-layer hybrid lattice was created by finding the $U = 0$ isosurface of

$$U_{\text{hyb.}} = \gamma U_{\text{hon [001]}} + (1 - \gamma) U_{\text{hon [100]}}, \tag{15}$$

where γ is a weighting distribution, and $U_{\text{hon [001]}}$ and $U_{\text{hon [100]}}$ are the surface functions of the honeycomb gyroid in each orientation. γ took the form of a 3D double sigmoid function, which varied between values of 0 in the lower and upper thirds of the structure, and 1 in the middle. The two-layer hybrid lattice was created in the same way, but with γ being a single sigmoid function centred at the mid-height of the structure.

It was previously reported by Maskery et al. [53] that transitions between two lattice types may result in an interfacial hybrid region with reduced load-bearing capacity. Those authors put forward an approach to correct for this by modifying the volume fraction in the interfacial hybrid region. In this work that approach is extended to the example of a three-layer hybrid lattice.

The three-layer hybrid lattice is shown in Fig. 13(a). The target volume fraction for the structure was 0.15, so the average relative cross-sectional from the base to the top of the structure should also be 0.15. The structural connectivity in the two interfacial hybrid regions was diminished, leading to a minimum relative cross-sectional area in the *xy*-plane of just 0.02, as seen in Fig. 13(b). The cross-sectional area over the full height of the structure was fit with two Gaussian peaks, one centred in each of the interfacial hybrid regions. The magnitudes of these peaks were then inverted to provide a volume fraction correction profile. Finally, the three-layer hybrid structure was re-generated using Eq. (15) with the volume fraction distribution determined by the correction profile. The minimum relative cross-sectional area in the hybrid regions was increased fourfold to 0.08, which is equivalent to the lowest cross-sectional area in the non-hybrid regions.

Deformation of the three-layer hybrid honeycomb lattice under compressive loading is shown in Fig. 14, and the corresponding stress-strain curve is given in Fig. 15. At low strain, all of the observed deformation was in the low-stiffness [100] regions. The initial elastic response and plastic plateau are identified as (*a*) and (*b*) on the stress–-strain curve. At $\varepsilon \approx 0.2$ (*c*), the cell walls completed their bending and rotation into the stiffer configuration described in Section 3.1. Above $\varepsilon \approx 0.35$ (*d*), the structure became extremely stiff as the [100] regions at the bottom and top of the structure entered densification. The densification mechanism exists for all cellular structures at high strain, but in this case it was localised to the [100] regions only, and at relatively low strain. The three-layer hybrid lattice then underwent weakening (*e*), likely due to the total plastic collapse of the [100] regions. At $\varepsilon > 0.65$ (*f*), the stiffness increased as the compressive load was transferred solely through the remaining high-stiffness [001] region.

The two-layer ([100]/[001]) hybrid structure deformed similarly to the three-layer hybrid, and the same (*a-f*) labeling is used in Fig. 15 to identify the deformation processes. The main distinction was that (*c–f*) occurred at lower strains in the two-layer hybrid structure.

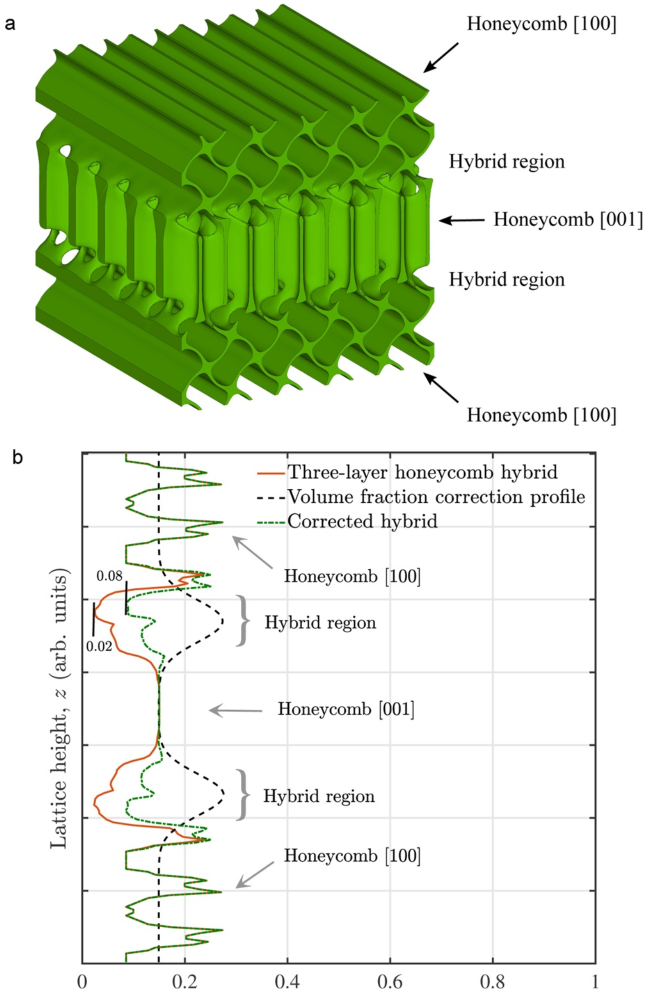

Fig. 13. Illustration of the three-layer honeycomb gyroid lattice structure (a) and a representation of its varying solid cross-sectional area (b).

It should be noted that the honeycomb regions of the two- and three-layer hybrid structures do not possess the same 5 × 5 periodicity as the honeycombs examined in Sections 3.1–3.3. For this reason, the stiffness and strength of the hybrid and non-hybrid lattice structures are not directly compared here. Rather, the hybrid structures illustrate how new deformation profiles may be enabled by expanding AM design freedom to include multiple cellular orientations.

4. Discussion

Regarding the mechanical properties of the network, matrix and honeycomb gyroid lattices, there are several results of note. The first, made clear in Fig. 10, is that the anisotropy of each lattice type has a very different dependence on the volume fraction, ρ^*. The anisotropy of each lattice type decreased with increasing ρ^* but, for example, while α_r for the matrix gyroid lattice remained fairly constant (and close to unity) over the examined range of $\rho^* = 0.1$–0.4, A^U for the honeycomb gyroid lattice decreased from 436 to 8 over the same range. Since ρ^* is the primary design variable for specifying the mechanical properties of AM lattices, it is clearly of some importance for the development of effective AM design approaches that a measure of anisotropy (i.e., $\alpha_r(\rho^*)$, $A^U(\rho^*)$, $E^*_{\text{max}}/E^*_{\text{min}}(\rho^*)$ or similar) be determined for a range of lattice types over a wide range of volume fractions. In this way, the

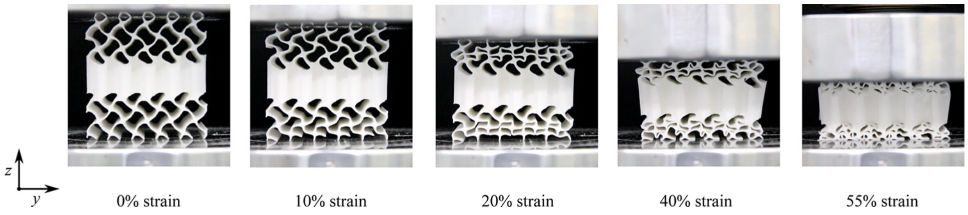

Fig. 14. Deformation of the three-layer hybrid honeycomb lattice under compressive loading.

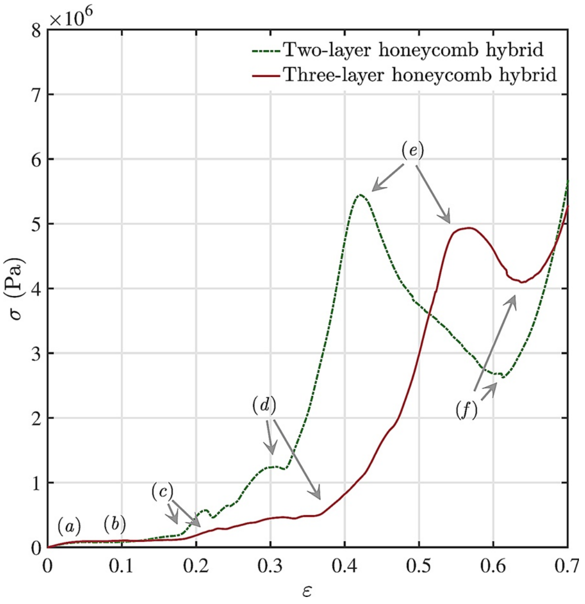

Fig. 15. Stress–strain curves of the two-layer and three-layer hybrid honeycomb lattices.

mechanical response of lattice structures to uni- or multi-axial loading may be predicted more accurately, and cellular orientation may be more effectively used as a design variable to maximise lattice stiffness for a given mass.

Second, the anisotropy of the honeycomb gyroid lattice examined in Sections 3.1–3.3 is very large. Taking the volume fraction 0.15, by the numerical homogenisation method it was found that $\alpha_r = 40$, $A^U = 129$ and $E^*_{\max}/E^*_{\min} = 224$, and by the compression testing of fabricated specimens it was found that $E^*_{\max}/E^*_{\min} \approx 250$. For comparison, the largest α_r reported for a TPMS-based lattice at $\rho^* = 0.15$ is approximately 4.5 [30], and the largest reported $E^*_{\max}/E^*_{\min}$ is 18.2 [28], though this latter result has $\rho^* = 0.1$. Further relevant comparison can be made with the square honeycomb using the analytic solution for E^*_{dia}, as given in Eq. (13), and the general result for all honeycombs that the out-of-plane modulus is equal to ρ^*; these give $E^*_{\max}/E^*_{\min} \approx 178$ for the square honeycomb at $\rho^* = 0.15$. Therefore, using the $E^*_{\max}/E^*_{\min}$ metric, the honeycomb gyroid has greater anisotropy than its closest analogue in the set of conventional honeycomb types. On the other hand, the *in-plane* stiffness anisotropy of the honeycomb gyroid is actually lower than that of the square honeycomb.

For the design of mechanical components, the large anisotropy of the honeycomb gyroid lattice could exclude it from applications in which high multi-axial stiffness is required, or when there is large variance or unpredictability in the loading direction, in which cases the matrix gyroid would be more appropriate. On the other hand, the honeycomb gyroid lattice is significantly stiffer in a single loading direction than the more commonly studied triply periodic lattice types.

Figs. 5, 7 and 8 show that the deformation of the honeycomb gyroid lattice under [100] loading is dissimilar from that of other AM lattice types in general. Due to its 2D periodicity and unique cell geometry, which features curved walls of non-uniform thickness, the honeycomb gyroid lattice takes on a second, stiffer configuration when the structure is loaded beyond its plastic plateau. This is due to the transition from bending- to stretching-dominated deformation following the contact of neighbouring cell walls. This is further illustrated in the compression of two- and three-layer hybrid lattice structures based on the honeycomb gyroid (Figs. 14 and 15). These structures underwent a sequence of deformation, stiffening and failure processes, with the choice of two or three layers providing a significant difference in the observed stress-strain response. This response differed greatly from the deformation of the non-hybrid, single-orientation honeycomb gyroid even though the structures had equivalent mass. A distinguishing feature of the multi-layer hybrid structures compared to other cellular structures made of elastic-plastic materials is the absence of long plastic plateaux in their stress-strain curves; for example, those seen for the network and matrix gyroid lattices in Fig. 5. Instead the hybrids exhibited a short plateau at low strain followed by phases of stiffening and collapse (as described more fully in Section 3.4).

The new honeycomb gyroid lattice, as well as hybrid versions of it, could be used to engineer more complex deformation and stress-strain responses in AM structures than is possible with the currently available array of lattice types. One application for such structures is lightweight armour panels. For such an application, the latticed core of the armour panel may be designed to control the deceleration of an impactor (e.g., a projectile) and provide post-yield stiffening just prior to its total penetration. In this way, the initial plastic deformation of the latticed core absorbs some kinetic energy of the impactor, while post-yield stiffening at high strain acts to prevent penetration, and therefore protect the user or shielded object from harm or damage. The use of hybrid honeycomb structures composed of high- and low-stiffness regions (such as the [001] and [100] regions examined here) would in this case provide a degree of control over the structural stiffness, *and* energy absorption, that would not be possible without this approach.

As a final point, there are as yet no examples in the literature of the honeycomb gyroid lattice being fabricated by a metal AM process, such as laser powder bed fusion, nor indeed by any process other than the polymer laser sintering used here. Each combination of material, structure and AM process presents different restrictions on manufacturability (minimum feature dimensions, overhangs, etc.) as well as a potentially unique microstructure which influences the mechanical properties. It is therefore clear that the honeycomb gyroid, and indeed the associated new family of reduced periodicity TPMS-based honeycomb structures, should be subject to further study using other AM processes. This will provide the information about their general performance which is required for their successful design and incorporation into advanced AM components.

5. Conclusions

Three gyroid-based lattice structures were investigated with numerical modelling and compression testing. Useful information about their anisotropy, structural deformation and post-yield stiffening was obtained. Information of this kind is required so that lattice structures, and AM components generally, may be designed to provide the required mechanical performance with the most efficient use of material.

Of the thee examined lattice types, the 2D honeycomb gyroid represents a new contribution to the field of AM lattice research, having not been presented previously. Volume fraction was found to provide a particularly sensitive control parameter for the anisotropy of this new honeycomb, and its deformation under in-plane loading was marked by a unique reorientation into a second, stiffer geometry following the plastic bending and contact of its cell walls. The honeycomb gyroid exhibited extremely high stiffness anisotropy, though interestingly its in-plane anisotropy is lower than that of the square honeycomb, its closest analogue in the set of conventional honeycomb types.

There is scope with the honeycomb gyroid lattice to provide post-yield stiffening at a pre-defined strain, as well as tailorable and progressive failure modes, through control of its volume fraction and the use of multi-orientation hybrid layers. These features make it particularly attractive for applications such as blast or projectile protection, where it is favourable to control both the structural stiffness and the rate of energy absorption under dynamic loading.

The gyroid-based honeycomb is part of a new family of 2D structures based on modified TPMS equations. These surface-based honeycombs are yet to be investigated, but they may prove a useful addition to the range of lattices generally considered for AM applications, providing very low weight solutions where high uniaxial stiffness is required. They may also be found, like the honeycomb gyroid examined here, to exhibit novel responses to mechanical loading. Lastly, being based on modified TPMS equations as opposed to connected struts or walls, AM surface-based honeycombs provide the potential for functional grading and general volume fraction control; this constitutes a key benefit compared to conventionally manufactured honeycombs.

Conflict of interest

None declared.

Declaration of Competing Interest

The authors report no declarations of interest.

Acknowledgments

This work was supported by the University of Nottingham(via Nottingham Research Fellowship funding).

References

[1] L.J. Gibson, M.J. Ashby, Cellular Solids: Structure and properties, Cambridge University Press, 1997.

[2] M.F. Ashby, A.G. Evans, N.A. Fleck, L.J. Gibson, L.W. Hutchinson, H.G. Wadley, Metal Foam: A Design Guide, Butterworth-Heinemann, 2000.

[3] R.A.W. Mines, S. Tsopanos, Y. Shen, R. Hasan, S.T. McKown, Drop weight impact behaviour of sandwich panels with metallic micro lattice cores, Int. J. Impact Eng. 60 (2013) 120–132.

[4] A. Beharic, R.R. Egui, L. Yang, Drop-weight impact characteristics of additively manufactured sandwich structures with different cellular designs, Mater. Des. 145 (2018) 122–134.

[5] H.N.G. Wadley, D.T. Queheillalt, Thermal applications of cellular lattice structures, THERMEC 2006, vol. 539 of Materials Science Forum, Trans Tech Publications, 2007, pp. 242–247 2.

[6] M. Wong, I. Owen, C.J. Sutcliffe, A. Puri, Convective heat transfer and pressure losses across novel heat sinks fabricated by selective laser melting, Int. J. Heat Mass Transfer 52 (1) (2009) 281–288.

[7] C. Mota, D. Puppi, F. Chiellini, E. Chiellini, Additive manufacturing techniques for the production of tissue engineering constructs, J. Tissue Eng. Regen. M 9 (3) (2012) 174–190.

[8] X.-Y. Zhang, G. Fang, J. Zhou, Additively manufactured scaffolds for bone tissue engineering and the prediction of their mechanical behavior: a review, Materials 10 (1) (2017).

[9] T. Wu, S. Yu, D. Chen, Y. Wang, Bionic design, materials and performance of bone tissue scaffolds, Materials 10 (10) (2017).

[10] S.M. Giannitelli, D. Accoto, M. Trombetta, A. Rainer, Current trends in the design of scaffolds for computer-aided tissue engineering, Acta Biomater. 10 (2) (2014) 580–594.

[11] K.H. Matlack, A. Bauhofer, S. Krödel, A. Palermo, C. Daraio, Composite 3d-printed metastructures for low-frequency and broadband vibration absorption, Proc. Natl. Acad. Sci. U.S.A. 113 (30) (2016) 8386–8390.

[12] X. Wang, P. Zhang, S. Ludwick, E. Belski, A.C. To, Natural frequency optimization of 3d printed variable-density honeycomb structure via a homogenization-based approach, Addit. Manuf. 20 (2018) 189–198.

[13] K. Hur, R.G. Hennig, U. Wiesner, Exploring periodic bicontinuous cubic network structures with complete phononic bandgaps, J. Phys. Chem. C 121 (40) (2017) 22347–22352.

[14] W. Elmadih, W.P. Syam, I. Maskery, D. Chronopoulos, R. Leach, Mechanical vibration bandgaps in surface-based lattices, Addit. Manuf. 25 (2019) 421–429.

[15] W. Elmadih, D. Chronopoulos, W.P. Syam, I. Maskery, H. Meng, R.K. Leach, Three-dimensional resonating metamaterials for low-frequency vibration attenuation, Sci. Rep. 9 (1) (2019) 11503.

[16] Y. Kok, X. Tan, P. Wang, M. Nai, N. Loh, E. Liu, S. Tor, Anisotropy and heterogeneity of microstructure and mechanical properties in metal additive manufacturing: a critical review, Mater. Des. 139 (2018) 565–586.

[17] U. Ajoku, N. Saleh, N. Hopkinson, R. Hague, P. Erasenthiran, Investigating mechanical anisotropy and end-of-vector effect in laser-sintered nylon parts, Proc. Inst. Mech. Eng. B.-J. Eng. 220 (7) (2006) 1077–1086.

[18] S. Ahn, M. Montero, D. Odell, S. Roundy, P.K. Wright, Anisotropic material properties of fused deposition modeling ABS, Rapid Prototyp. J. 8 (4) (2002) 248–257.

[19] J.R.C. Dizon, A.H. Espera, Q. Chen, R.C. Advincula, Mechanical characterization of 3d-printed polymers, Addit. Manuf. 20 (2018) 44–67.

[20] H. Alsalla, L. Hao, C. Smith, Fracture toughness and tensile strength of 316L stainless steel cellular lattice structures manufactured using the selective laser melting technique, Mater. Sci. Eng. A-Struct. 669 (2016) 1–6.

[21] V. Weißmann, R. Bader, H. Hansmann, N. Laufer, Influence of the structural orientation on the mechanical properties of selective laser melted Ti6Al4V open-porous scaffolds, Mater. Des. 95 (2016) 188–197.

[22] M. Simonelli, Y.Y. Tse, C. Tuck, Effect of the build orientation on the mechanical properties and fracture modes of SLM Ti-6Al-4V, Mater. Sci. Eng. A-Struct. 616 (2014) 1–11.

[23] B.E. Carroll, T.A. Palmer, A.M. Beese, Anisotropic tensile behavior of Ti-6Al-4V components fabricated with directed energy deposition additive manufacturing, Acta Mater. 87 (2015) 309–320.

[24] Q. Zhang, J. Chen, Z. Zhao, H. Tan, X. Lin, W. Huang, Microstructure and anisotropic tensile behavior of laser additive manufactured TC21 titanium alloy, Mater. Sci. Eng. A-Struct. 673 (2016) 204–212.

[25] S. Xu, J. Shen, S. Zhou, X. Huang, Y.M. Xie, Design of lattice structures with controlled anisotropy, Mater. Des. 93 (2016) 443–447.

[26] G. Dong, Y. Tang, Y.F. Zhao, A 149 line homogenization code for three-dimensional cellular materials written in matlab, J. Eng. Mater.-Trans. ASME 141 (1) (2018) 011005.

[27] A. Cutolo, B. Engelen, W. Desmet, B. Van Hooreweder, Mechanical properties of diamond lattice Ti-6Al-4V structures produced by laser powder bed fusion: on the effect of the load direction, J. Mech. Behav. Biomed. Mater. 104 (2020) 103656.

[28] T. Tancogne-Dejean, D. Mohr, Stiffness and specific energy absorption of additively-manufactured metallic BCC metamaterials composed of tapered beams, Int. J. Mech. Sci. 141 (2018) 101–116.

[29] Y. Lu, W. Zhao, Z. Cui, H. Zhu, C. Wu, The anisotropic elastic behavior of the widely-used triply-periodic minimal surface based scaffolds, J. Mech. Behav. Biomed. Mater. 99 (2019) 56–65.

[30] C. Soyarslan, V. Blümer, S. Bargmann, Tunable auxeticity and elastomechanical symmetry in a class of very low density core-shell cubic crystals, Acta Mater. 177 (2019) 280–292.

[31] I. Maskery, A. Hussey, A. Panesar, A. Aremu, C. Tuck, I. Ashcroft, R. Hague, An investigation into reinforced and functionally graded lattice structures, J. Cell. Plast. 53 (2) (2017) 151–165.

[32] S. Yu, J. Sun, J. Bai, Investigation of functionally graded TPMS structures fabricated by additive manufacturing, Mater. Des. 182 (2019) 108021.

[33] I. Maskery, N.T. Aboulkhair, A.O. Aremu, C.J. Tuck, I.A. Ashcroft, R.D. Wildman, R.J.M. Hague, A mechanical property evaluation of graded density Al-Si10-Mg lattice structures manufactured by selective laser melting, Mater. Sci. Eng. A-Struct. 670 (2016) 264–274.

[34] W. van Grunsven, E. Hernandez-Nava, G.C. Reilly, R. Goodall, Fabrication and mechanical characterisation of titanium lattices with graded porosity, Metals 4 (2014) 401–409.

[35] G. Singh, P.M. Pandey, Uniform and graded copper open cell ordered foams fabricated by rapid manufacturing: surface morphology, mechanical properties and energy absorption capacity, Mater. Sci. Eng. A 761 (2019) 138035.

[36] D. Li, W. Liao, N. Dai, Y.M. Xie, Comparison of mechanical properties and energy absorption of sheet-based and strut-based gyroid cellular structures with graded densities, Materials 12 (13) (2019).

[37] I. Maskery, L. Sturm, A.O. Aremu, A. Panesar, C.B. Williams, C.J. Tuck, R.D. Wildman, I.A. Ashcroft, R.J.M. Hague, Insights into the mechanical properties of several triply periodic minimal surface lattice structures made by polymer additive manufacturing, Polymer 152 (2018) 62–71.

[38] I. Maskery, N.T. Aboulkhair, A.O. Aremu, C.J. Tuck, I.A. Ashcroft, Compressive failure modes and energy absorption in additively manufactured double gyroid lattices, Addit. Manuf. 16 (2017) 24–29.

[39] J. Weidmann, A. Großmann, C. Mittelstedt, Laser powder bed fusion manufacturing of aluminum honeycomb structures: theory and testing, Int. J. Mech. Sci. 180 (2020) 105639.

[40] X. Zheng, H. Lee, T.H. Weisgraber, M. Shusteff, J. DeOtte, E.B. Duoss, J.D. Kuntz, M.M. Biener, Q. Ge, J.A. Jackson, S.O. Kucheyev, N.X. Fang, C.M. Spadaccini, Ultralight, ultrastiff mechanical metamaterials, Science 344 (6190) (2014) 1373–1377.

[41] V.S. Deshpande, N.A. Fleck, M.F. Ashby, Effective properties of the octet-truss

lattice material, J. Mech. Phys. Sol. 49 (8) (2001) 1747–1769.
[42] P.J.F. Gandy, S. Bardhan, A.L. Mackay, J. Klinowski, Nodal surface approximations to the P, G, D and I-WP triply periodic minimal surfaces, Chem. Phys. Lett. 336 (3) (2001) 187–195.
[43] O. Al-Ketan, R. Rowshan, A.N. Palazotto, R.K. Abu Al-Rub, On mechanical properties of cellular steel solids with shell-like periodic architectures fabricated by selective laser sintering, J. Eng. Mater. Technol. 141 (2) (2019).
[44] S.C. Kapfer, S.T. Hyde, K. Mecke, C.H. Arns, G.E. Schr”oder-Turk, Minimal surface scaffold designs for tissue engineering, Biomaterials 32 (29) (2011) 6875–6882.
[45] O. Al-Ketan, R. Rowshan, R.K.A. Al-Rub, Topology-mechanical property relationship of 3D printed strut, skeletal, and sheet based periodic metallic cellular materials, Addit. Manuf. 19 (2018) 167–183.
[46] L. Zhang, S. Feih, S. Daynes, S. Chang, M.Y. Wang, J. Wei, W.F. Lu, Energy absorption characteristics of metallic triply periodic minimal surface sheet structures under compressive loading, Addit. Manuf. 23 (2018) 505–515.
[47] S.C. Han, J.W. Lee, K. Kang, A new type of low density material: shellular, Adv. Mater. 27 (37) (2015) 5506–5511.
[48] B.D. Nguyen, S.C. Han, Y.C. Jung, K. Kang, Design of the P-surfaced shellular, an ultra-low density material with micro-architecture, Comput. Mater. Sci. 139 (2017) 162–178.
[49] E. Andreassen, C.S. Andreasen, How to determine composite material properties using numerical homogenization, Comput. Mater. Sci. 83 (2014) 488–495.
[50] C.H.P. Nguyen, Y. Kim, Y. Choi, Design for additive manufacturing of functionally graded lattice structures: a design method with process induced anisotropy consideration, Int. J. Precis. Eng. Manuf.-Green Technol. (2019).
[51] D.B. Ngim, J.-S. Liu, R.C. Soar, Design optimization of consolidated granular-solid polymer prismatic beam using metamorphic development, Int. J. Solids Struct. 46 (3) (2009) 726–740.
[52] Z. Chen, Y.M. Xie, X. Wu, Z. Wang, Q. Li, S. Zhou, On hybrid cellular materials based on triply periodic minimal surfaces with extreme mechanical properties, Mater. Des. 183 (2019) 108109.
[53] I. Maskery, A.O. Aremu, L. Parry, R.D. Wildman, C.J. Tuck, I.A. Ashcroft, Effective design and simulation of surface-based lattice structures featuring volume fraction and cell type grading, Mater. Des. 155 (2018) 220–232.
[54] C. Zener, Contributions to the theory of beta-phase alloys, Phys. Rev. 71 (12) (1947) 846–851.
[55] EOS, Polyamide 12 for 3D Printing. https://www.eos.info/en/additive-manufacturing/3d-printing-plastic/sls-polymer-materials/polyamide-pa-12-alumide (Accessed 20 July 2020).
[56] A.-J. Wang, D.L. McDowell, In-plane stiffness and yield strength of periodic metal honeycombs, J. Eng. Mater. Technol. 126 (2) (2004) 137–156.
[57] S.I. Ranganathan, M. Ostoja-Starzewski, Universal elastic anisotropy index, Phys. Rev. Lett. 101 (2008 Aug) 055504.